

Avoiding Dense and Dynamic Obstacles in Enclosed Spaces: Application to Moving in a Simulated Crowd

Lukas Huber¹ · Jean-Jacques Slotine² · Aude Billard¹

Abstract—This paper presents a closed-form approach to constrain a flow within a given volume and around objects. The flow is guaranteed to converge and to stop at a single fixed point.

We show that the obstacle avoidance problem can be inverted to enforce that the flow remains enclosed within a volume defined by a polygonal surface. We formally guarantee that such a flow will never contact the boundaries of the enclosing volume and obstacles, and will asymptotically converge towards an attractor. We further create smooth motion fields around obstacles with edges (e.g. tables).

The technique to enable a robot to navigate within an enclosed corridor while avoiding static and moving obstacles. It is applied on an autonomous robot (QOLO) in a static complex indoor environment, and also tested in simulations with dense crowds.

I. INTRODUCTION

Robots navigating in human-inhabited environments will encounter disturbances constantly, for instance when pedestrians walk around autonomous delivery robots. To avoid collisions, the robot must have a flexible control scheme. As the number of obstacles increase and their motion becomes less predictable, the robot needs to reevaluate its path within milliseconds to avoid a crash, while moving actively towards its goal.

Control using dynamical systems (DS) is ideal to address such situations. In contrast to classical path planning, the control law is closed-form, hence requires no re-planning, and can ensure impenetrability of obstacles [1], [2]. DS, thus, offer stability and convergence guarantees in addition to the desired on-the-fly re-activity.

Sampling algorithms such as probabilistic road map (PRM) [3] or the rapidly exploring random trees (RRT) [4] can find a path in cluttered environments, but they are computationally slow and limited to static environments. Online (partial) replanning and elastic-band methods deform locally the path have extended the approaches to dynamic environments [5], [6]. However, this switching comes with lose of global convergence [7]. Recent work use customized circuitry on a chips for on-board global sampling and evaluation of all paths [8]. Path sampling methods are not suitable for dynamic environments due to computational time. We introduce an closed-form algorithm which is able to evaluates and reacts to the environment in

real-time.

With improvements in hardware and computational speed, optimization algorithm such as model predictive control (MPC) have become feasible for on-board use in dynamic path planning and obstacle avoidance [9]. MPC has been applied on non-holonomic obstacles for environment which have to be described as a union of convex obstacles [10]. A recent approach uses power diagrams to identify the robot's collision free, convex neighbourhood and an associated, well-known convex optimization problem generates a continuous flow [11]. This method is limited to convergence for convex obstacles almost spherical curvature. Both methods guarantee convergence in only simple, local environments.

In the past years, machine learning algorithms have been applied to sensor data to infer data-driven control [12], but later cannot ensure impenetrability. Other approaches use neural networks on a circular representation of crowds to create steering laws [13]. Neither is able to ensure convergence.

Many local methods for obstacle avoidance are based on artificial potential fields [14], [15]. These algorithm often create (topologically) avoidable local minimum [16]. Using quadratic potential functions allowed to obtain full convergence around ellipse obstacles [17]. Learning methods have been used to tune the hyper-parameters of potential fields to obtain human-inspired behavior for obstacle avoidance of learned motion [18]. Navigation functions allow to transform static environments of *trees of stars-shapes* into simpler environments where all obstacle-trees are reduced to spheres [19]. In these transformed world, the artificial potential fields lead to converging vector-fields [20]. Other approaches further reduces the space to a *point-world* [21] and apply navigation function based on harmonic potentials in planar space [22]. Navigation function were able to elevate the concept of potential functions to complex environments, but their construction is hard and limited to static environments.

Harmonic potential functions are particularly interesting as they guarantee that no topologically critical points arise in free space. However, as they are hard to find, potential functions are often evaluated numerically [23]. Closed-form harmonic potential functions can be generated by approximating the obstacles through linear *panels* [24]. This allows to treat concave obstacles, but is limited to static environments [1]. In other attempts, harmonic potential function are found for convex obstacles by using sliding mode between them [25]. This can be extended to linearly moving and rotating obstacles,

*This work was funded in part by the EU ERC grant SAHR.

¹ LASA Laboratory, Swiss Federal School of Technology in Lausanne - EPFL, Switzerland. {lukas.huber;aude.billard}@epfl.ch

² Nonlinear Systems Laboratory, Massachusetts Institute of Technology, USA. jjs@mit.edu

but is limited to two dimensions [1]. A closed-form solution of harmonic potential flow around simple obstacles was presented in [26]. While the work ensures to avoid moving obstacles, it was restricted to convex obstacles. An extension to concave obstacles using discrete, sensor-based representation was offered in [27]. Many previous implementations of obstacle avoidance algorithm are simplified to circular world or require high (close to circular) curvature.

The velocity obstacle approach [28] allows to navigate in dynamic environments by creating analysing the possible velocities with respect to another agent. This could is often used in multi-agent cases [29] and could be extended to consider include acceleration and non-holonomic constraints of the agent [30]. The velocity obstacle approach often limits the work space, we propose a less conservative approach by evaluating in the frame of the obstacle.

Dynamic reference points placement to establish state dependent potential field help increase the convergence for potential fields [31]. In combination with dynamical systems this could be extended to *star-shaped* obstacles with smooth boundaries [32]. This work allowed a fast and closed-form description for many environments, but it does not handle boundaries of the space.

Contributions: We address the need to have a reactive obstacle avoidance approach, in closed-form with formal guarantees of non-penetrability, to handle highly dynamic environments and realistic obstacles, such as obstacles with sharp edges. To this end, this paper extends our previous work [32], in which we presented a closed-form obstacle avoidance approach guaranteed to not penetrate smooth concave, albeit star-shaped, obstacles. We present three novel theoretical contributions: 1) We invert the obstacle description and by so doing ensure that the robot moves within the enclosed space defined by the boundary, while preserving stability guarantees at an attractor. This boundary may represent walls, furniture or joint limits of manipulators (Sec. IV). 2) We extend the approach to handle to *non-smooth* concave and convex surfaces, i.e. with sharp edges. The novelty comes from creating a smooth dynamical system around an obstacle without approximation of the curvature (Sec. V). 3) We show that the approach can be extended to tackle dynamic environments, with obstacles that have *deforming* shapes (Sec. VI)

We validate these contributions with a wheel-chair robot moving in a simulated crowd of pedestrians and in an office world with real furniture. To enable real-world implementation of the approach, we propose two additional technical contributions: we introduce a general directional weighting for (ensured) non-trivial summing of vector fields (Sec. II), and a corresponding gradient descend (Sec. VII). We also propose new modulation parameters (surface friction and repulsive value) which allow an agent to move slower and further away from obstacles, respectively. This results in more cautious behavior, which we believe is desirable when robot moves around pedestrians.

While the experimental implementation is executed on a autonomous wheel chair, a two dimensional scenario, this work provides a theoretical solution, which is not limited to 2D world and could be applied to higher dimensional spaces.

II. PRELIMINARIES

$\xi \in \mathbb{R}^d$ is the state of the robotic system whose dynamics is governed by a dynamical system (DS) which is autonomous (time invariant) and linear with a single attractor ξ^a of the form:

$$\mathbf{f}(\xi) = -k(\xi)(\xi - \xi^a) \quad (1)$$

with $k(\xi) \in \mathbb{R}_{>0}$ a position dependent scaling factor.

A. Obstacle Description

Similar to [32], we define for each obstacle a continuous distance function $\Gamma(\xi) : \mathbb{R}^d \setminus \mathcal{O} \mapsto \mathbb{R}_{\geq 1}$, which allows to distinguish three regions:

$$\begin{aligned} \text{Free points:} & \quad \mathcal{F} = \{\xi \in \mathbb{R}^d : \Gamma(\xi) > 1\} \\ \text{Boundary points:} & \quad \mathcal{B} = \{\xi \in \mathbb{R}^d : \Gamma(\xi) = 1\} \\ \text{Interior points:} & \quad \mathcal{I} = \{\xi \in \mathbb{R}^d \setminus (\mathcal{F} \cup \mathcal{B})\} \end{aligned} \quad (2)$$

For each obstacle i a reference point inside the obstacle $\xi^r \in \mathcal{I}$ can be defined. The reference direction is the radial direction towards the state of the robotic system with respect to the reference point:

$$\mathbf{r}(\xi) = (\xi - \xi^r) / \|\xi - \xi^r\| \quad \forall \xi \in \mathbb{R}^d \setminus \xi^r \quad (3)$$

By construction, the distance function $\Gamma(\cdot)$ increases monotonically in radial direction and has a continuous first-order partial derivative (C^1 smoothness). Here, we define it for general obstacles as:

$$\Gamma^o(\xi) = (\|\xi - \xi^r\| / R(\xi))^{2p} \quad \forall \xi \in \mathbb{R}^d \setminus \xi^r \quad (4)$$

with the power $p \in \mathbb{N}_+$ with the local radius $R(\xi) = \|\xi^b - \xi^r\|$ as a function of the surface point:

$$\xi^b = b\mathbf{r}(\xi) + \xi^r \quad \text{such that } b > 0, \xi^b \in \mathcal{B} \quad (5)$$

1) *Star shape:* The present algorithm uses star shaped obstacles, i.e. an obstacle which has a reference point within its boundary, such that the reference direction is linearly independent of the tangent for any point on the surface, i.e.

$$\langle \mathbf{r}(\xi), \mathbf{n}(\xi) \rangle > 0 \quad \forall \xi \in \mathcal{E}, \exists \xi^r \in \mathcal{I} \quad (6)$$

where $\mathbf{n}(\xi)$ the normal is evaluated at the edge of a surface \mathcal{E} as in (5).

B. Directional Weighted Mean

The weighted summation of vectors can result in a zero sum, e.g. two vectors opposing each other with equal weight. If the sum of the vectors is a dynamical system for a robot motion, this can lead to local minima and undesired stopping of the agent. If the vector is used in an algorithm, the system might not be defined anymore.

This problem can be resolved by summing in directional space, similarly as in [32]. Let us define a general direction as:

$$\{\mathbf{v} \in \mathbb{R}^d : \|\mathbf{v}\| = 1\} \quad (7)$$

The transformation into direction space \mathcal{K}^π is given by:

$$\mathcal{K}^\pi = \{\boldsymbol{\kappa} \in \mathbb{R}^{d-1} : \|\boldsymbol{\kappa}\| < \pi\} \quad (8)$$

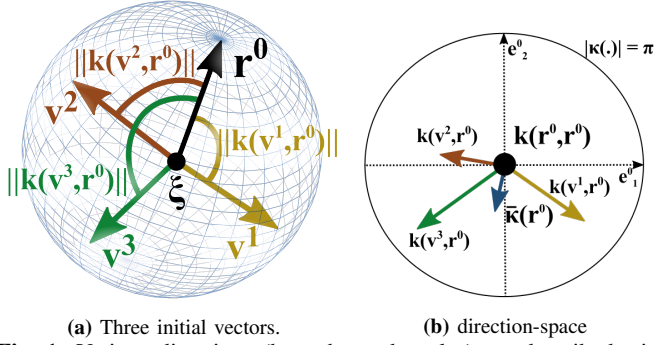


Fig. 1: Various directions (here three obstacles) are described with respect to a basis direction \mathbf{r}^0 . (a). The directions are transformed to κ -space (b) where the weighted mean, $\bar{\kappa}$, is obtained.

The direction space is with respect to a reference vector \mathbf{r}^0 which is the first column of the orthonormal transformation matrix:

$$\mathbf{R}^0 = [\mathbf{r}^0 \ \mathbf{e}_1^0 \ \dots \ \mathbf{e}_{d-1}^0] \quad (9)$$

This allows the transformation into the new basis:

$$\hat{\mathbf{v}}^i = (\mathbf{R}^0)^T \mathbf{v}^i \quad (10)$$

To evaluate the direction space, only the projections orthogonal to a reference vector are considered. The magnitude of the transformed vector in direction space is equal to the angle between the original vector and the reference vector. The transformation of the initial vector \mathbf{v}^i in the direction-space is:

$$\kappa^i(\mathbf{r}^0) = \mathbf{k}(\mathbf{v}^i, \mathbf{r}^0) = \begin{cases} \arccos(\hat{\mathbf{v}}_1^i) \frac{[\hat{\mathbf{v}}_2^i \ \dots \ \hat{\mathbf{v}}_d^i]^T}{\|[\hat{\mathbf{v}}_2^i \ \dots \ \hat{\mathbf{v}}_d^i]^T\|} & \text{if } \hat{\mathbf{v}}_1^i \neq 1 \\ \mathbf{0}^T & \text{if } \hat{\mathbf{v}}_1^i = 1 \end{cases} \quad (11)$$

The mean is evaluated as a function of the weight w^i of all N^v vectors:

$$\bar{\kappa} = \sum_{i=1}^{N^v} w^i \kappa^i \quad (12)$$

The reconstruction into original space is evaluated as:

$$\bar{\mathbf{v}} = \begin{cases} \mathbf{R}^0 \begin{bmatrix} \cos \|\bar{\kappa}\| & \sin \|\bar{\kappa}\| \frac{\bar{\kappa}}{\|\bar{\kappa}\|} \end{bmatrix}^T & \|\bar{\kappa}\| \neq 0 \\ \mathbf{R}^0 \begin{bmatrix} 1 & 0 & \dots & 0 \end{bmatrix}^T & \text{if } \|\bar{\kappa}\| = 0 \end{cases} \quad (13)$$

1) *Intuition:* In the two-dimensional case, this hyper-sphere is a line which represents the angle between the initial DS $f(\xi)$ and the modulated DS ξ_k . It has a magnitude strictly smaller than π . In higher dimensions (e.g. three dimensions in Fig. 1) the directional space is a vector-space, where the weighted mean is taken.

This transformation ensures that any weighted mean calculation of directions outputs a direction as defined in (7).

Theorem 1 Consider a unit vector \mathbf{r}^0 as the basis for the projection given in (11) and the corresponding reconstruction function defined in (13). The resulting transformation of unit vector $\mathbf{k}(\mathbf{v}, \mathbf{r}^0) : \{\mathbf{v} \in \mathbb{R}^d \setminus -\mathbf{r}^0 : \|\mathbf{v}\| = 1\} \rightarrow \mathcal{K}^\pi$ defined in (8) is a bijection and the basis vector projects to the origin, i.e. $\mathbf{r}^0 \rightarrow \mathbf{0}$.

Proof: see Appendix A.

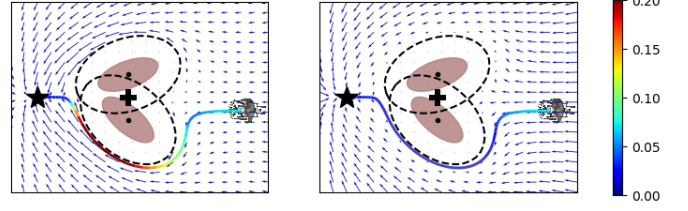


Fig. 2: The isometric inspired eigenvalue (left) induce unexpected accelerations in free space. The modulation inspired by surface friction (right) reduces the velocity with decreasing distance to the obstacle.

C. Smooth Vector field

Any path in a vector field is smooth, if the whole velocity flow is continuous, i.e.

$$\lim_{\xi_1 \rightarrow \xi_2} \mathbf{M}(\xi_1) \mathbf{f}(\xi_1) = \mathbf{M}(\xi_2) \mathbf{f}(\xi_2) \quad (14)$$

since $\mathbf{f}(\cdot)$ is continuous it is sufficient for $\mathbf{M}(\cdot)$ to be continuous. The modulation matrix is a function of three variables: the pseudo normal $\hat{\mathbf{n}}(\xi)$, the null-direction $\mathbf{r}(\xi)$, and the distance function $\Gamma(\xi)$. If all of them are continuously defined outside, continuity of the modulated DS follows.

III. OBSTACLE AVOIDANCE [32]

Real-time obstacle avoidance is obtained by applying a dynamic modulation matrix to the original DS given in (1):

$$\dot{\xi} = \mathbf{M}(\xi) \mathbf{f}(\xi) \quad \text{with} \quad \mathbf{M}(\xi) = \mathbf{E}(\xi) \mathbf{D}(\xi) \mathbf{E}(\xi)^{-1} \quad (15)$$

It is composed of a basis matrix:

$$\mathbf{E}(\xi) = [\mathbf{r}(\xi) \ \mathbf{e}_1(\xi) \ \dots \ \mathbf{e}_{d-1}(\xi)] \quad (16)$$

which has the orthonormal tangent vectors $\mathbf{e}_i(\xi)$ with $i = 1..d-1$ evaluated at the boundary point ξ^b given in (5).

The basis matrix $\mathbf{E}(\xi)$ has full rank (but is not necessarily orthonormal).

The diagonal eigenvalue matrix is given as:

$$\mathbf{D}(\xi) = \text{diag}(\lambda_r(\xi), \lambda_e(\xi), \dots, \lambda_e(\xi)) \quad (17)$$

Using the existence of $\Gamma(\xi)$ see (2), that measures the distance to the obstacle's surface, we set:

$$\lambda_r(\xi) = 1 - 1/\Gamma(\xi)^{1/\rho} \quad \lambda_e(\xi) = 1 + 1/\Gamma(\xi)^{1/\rho} \quad (18)$$

with the reactivity factor $\rho \in \mathbb{R}_{>0}$ and where $\Gamma(\xi)$ from (4) is defined and finite.

1) *Surface Friction Imitation:* The choice of eigenvalues in (18) are inspired by the harmonic potential flow, as it is to describe fluid motion. The eigenvalues in tangent direction are increasing as is observed in incompressible flow. This can have undesired acceleration close to the surface (see Fig. 2).

We therefore propose to additionally include a notion of friction on the surface, i.e. slowing down in tangent direction close to an obstacle ($\lim_{\Gamma \rightarrow 1} \xi_e \rightarrow 0$). A friction factor $\lambda_f(\xi)$ ensures the slowing down towards the surface. It has to be applied in tangent and reference direction:

$$\dot{\xi}_f = \lambda_f(\xi) \frac{\|\mathbf{f}(\xi)\|}{\|\dot{\xi}\|} \dot{\xi} \quad \text{with} \quad (19)$$

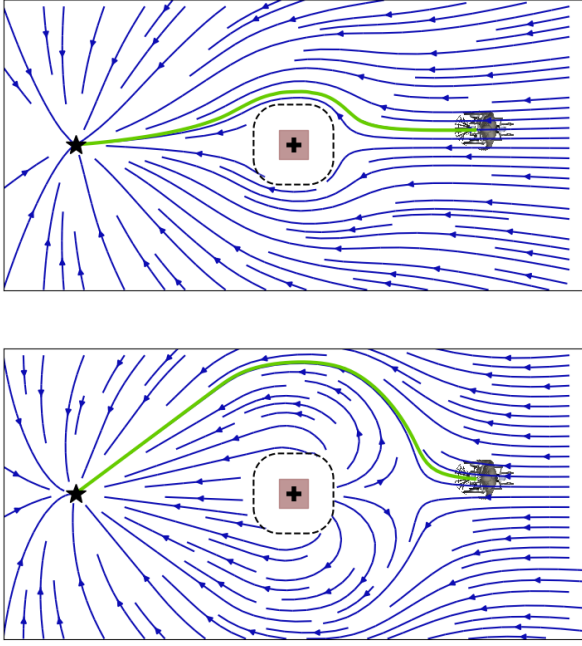


Fig. 3: A repulsion coefficient $c_{rep} = 1$ results in strictly positive eigenvalues (top). This allows the flow to move closer to the obstacle than with a repulsion coefficient $c_{rep} = 2$ where we encounter active repulsion in front of the obstacle (bottom).

2) *Repulsive Eigenvalue:* Positive eigenvalues in reference direction (as described above) decrease the flow towards an obstacle. A reversion of the flow, i.e. a repulsive effect, can be achieved by negative eigenvalue $\lambda(\xi)_r$. This increases the distance by which the robot avoids the obstacle (Fig. 3). This differs from simply increasing obstacle margin, as this does not create any dead space in clustered environments. The eigenvalue in normal direction is defined as:

$$\lambda_r(\xi) = \begin{cases} 1 - c_{rep}/\Gamma(\xi)^{1/\rho} & \text{if } \langle \mathbf{f}(\xi), \mathbf{r} \rangle < 0 \\ 1 & \text{otherwise} \end{cases} \quad (20)$$

with the repulsive coefficient $c_{rep} \geq 1$. A repulsive coefficient of one corresponds to no repulsion. The undesirable influence of the eigenvalue in reference direction behind the obstacle can be canceled using the *tail-effect* as introduced by [26].

3) *Reference Point:* The algorithm is based on a reference point $\mathbf{r}(\xi)$. It is a point within a star-shaped obstacle, from which in each direction there is only one surface point. For convex obstacles, it can be placed anywhere within the hull.

A. Multiple Obstacles

In the presence of multiple obstacles, the nominal DS is modified by taking the weighted mean of the modulated DS ξ^o created by each obstacle $o = 1..N^o$; separately for the magnitude $\|\xi^o\|$ and direction \mathbf{v}^{ξ^o} . The directional weighted mean is evaluated using the algorithm described in Sec. II-B, with the reference direction being along the initial DS $\mathbf{f}(\xi)$. The weight of each obstacle is a decreasing function of the distance function $\Gamma(\xi)$.

IV. INVERTED OBSTACLE AVOIDANCE

Autonomous robot often encounter scenarios where it has boundaries which it can not pass. This might be a wall for

wheeled robot or a flying drone inside. Conversely, it could also be joint limits for a robot arm. This problem can be seen as staying within an *obstacle*, where the boundary of the obstacle represent the limits of the free space.

A. Distance Inversion

The distance function $\Gamma(\xi)$ from (4) can be evaluated within the obstacle $\xi \in \mathcal{S}$.¹ For interior points, our boundary function is monotonically decreasing along the radial direction and bounded:

$$\frac{\partial \Gamma(\xi)}{\partial \mathbf{r}(\xi)} > 1, \quad \Gamma(\xi) \in [0, 1[\quad \forall \mathcal{S} \setminus \xi^r \quad (21)$$

If we consider the obstacle boundary \mathcal{X} as the description of an enclosing hull, the interior points of the classical obstacle become points of free space of the enclosing hull and vice versa. Boundary points stay boundary points. Defining the distance function of obstacles as the inverse of the obstacle distance function:

$$\Gamma^w(\xi) = 1/\Gamma^o = (R(\xi)/\|\xi - \xi^r\|)^{2p} \quad \forall \mathbb{R}^d \setminus \xi^r \quad (22)$$

results in a new distance function which again fulfills the condition for the three regions as given in (2) since on boundary $\Gamma = 1$. The distance function Γ is now monotonically decreasing along radial direction and reaches infinity at the reference point, i.e. $\lim_{\xi \rightarrow \xi^r} \Gamma^w(\xi) \rightarrow \infty$ (Fig. 7).

B. Modulation Matrix

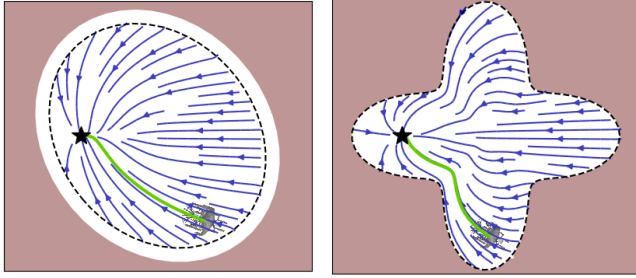
The modulation matrix in (15) consists of two parts. The diagonal eigenvalue matrix defined in (17), which can be evaluated using the Inverted distance function from (22). Conversely, the basis matrix is constant along radial direction, hence it is defined within the free space of enclosing walls except the reference point.

Theorem 2 Consider a star-shaped enclosing wall in \mathbb{R}^d with respect to a reference point inside the obstacle ξ^r as in (6) and a boundary $\Gamma^w(\xi) = 1$ as in (22). Any trajectory $\{\xi\}_t$, that starts within the free space of an enclosing wall, i.e. $\Gamma(\{\xi\}_0) > 1$ and evolves on a smooth path according to (15), will never reach the wall, i.e. $\Gamma(\{\xi\}_t) > 1, t = 0.. \infty$ and converges towards an attractor in free space $\xi^a \in \mathcal{F}$, i.e. $\lim_{t \rightarrow \infty} \xi \rightarrow \xi^a$. **Proof:** see Appendix B. ■

C. Guiding Reference Point to Pass Wall Gaps

In practical scenarios, it may happen that the hull entails gaps or holes (e.g. door in a room), through which we may want the agent to enter or exit the space enclosed by the boundary. While the obstacle avoidance approach we have develop would allow the agent to escape through the gap, it would lead the agent to slow down massively when approaching the exit as its velocity is meant to vanish when reaching the boundary. To counter this effect, we introduce a *guiding reference point* for boundary obstacles. For simplicity, we only look at convex gaps.

¹In the classic obstacle avoidance case, this is of no use, since theoretically the obstacle does never reach the boundary [32], and practically an *emergency* control has to be applied if such a case happens.



(a) Ellipsoid boundary (b) Star-shaped boundary

Fig. 4: A smooth flow with full convergence towards the attractor (black star) can be observed within any star-shaped wall with reference point ξ^r (black plus).

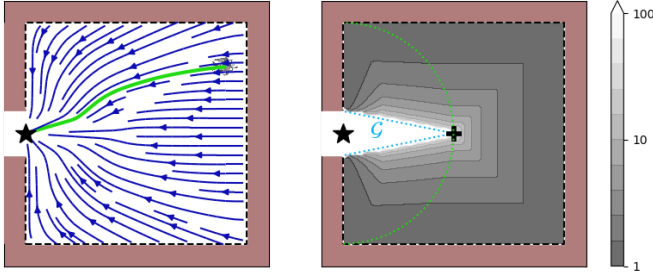


Fig. 5: Inside a boundary with gap and the use of a guiding reference point, the dynamical system (left) is not modulated in front of the gap since the Gamma-function reaches infinity (right). The edge of the set of gap points \mathcal{G} is limited by blue lines. The influence of the gap is limited by the green circle.

In Sec. IV-A, it was shown that at the center of the obstacle where the reference point and the agent's position align ($\xi_r = \xi$), there is no influence of the modulation, i.e. $\dot{\xi} = M(\xi)\mathbf{f}(\xi) = \mathbf{f}(\xi)$. The newly introduced guiding reference point $\mathbf{g}_r(\xi)$ changes position during the execution, similarly to a dynamic reference point. However, the guiding reference point is a function of the position (not of time).

Let us define the set of gap points \mathcal{G} , which includes all points which are enclosed by the connection of the gap edges and the reference point ξ_r (see Fig. 5).

The guiding reference point \mathbf{g}_r is equal to the reference point ξ_r when the robot is far away from the gap, so as to generate the same behavior as in a boundary without gap. In the region close to the gap, the guiding reference point \mathbf{g}_r is equal to the position of the evaluation, hence no influence of the modulation. In between the two regions, the guiding reference point is projected onto the gap region \mathcal{G} . This can be written as:

$$\xi_{r,g} = \begin{cases} \xi_r & \text{if } \|\xi_{c,g} - \xi\| > \|\xi_{c,g} - \xi_r\| \\ \xi & \text{else if } \xi \in \mathcal{G} \\ \operatorname{argmin}_{\xi_{r,g} \in \mathcal{G}} \|\xi - \xi_{r,g}\| & \text{otherwise} \end{cases}$$

V. NON-SMOOTH SURFACES

Human designed environment often contain obstacles and enclosing walls with non-smooth surfaces; from edged of tables to corners of rooms and buildings. While they could be approximated with a smooth surface of high gradient, this is often not desired. These edges are the most prone to collision as agents need to turn around those. A

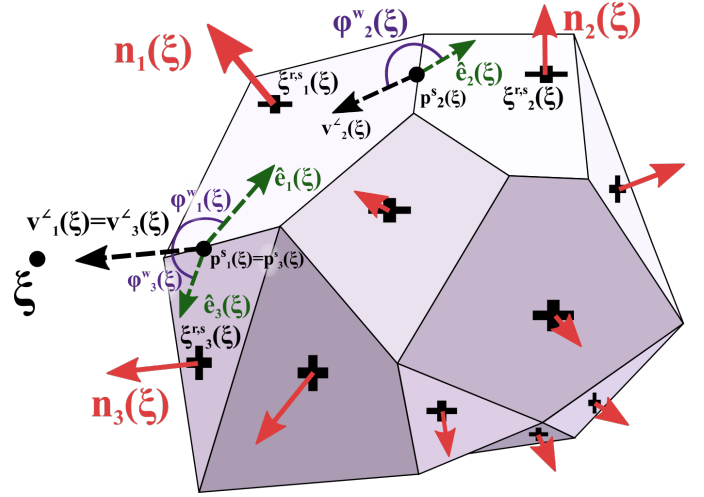


Fig. 6: The variables for the evaluation of the pseudo normal $\hat{\mathbf{n}}(\xi)$ of a non-smooth star-shaped obstacle are displayed for the first three surfaces. For the others only reference point (cross) and the surface normal (red arrow) are visualized. The angle ψ^w is always evaluated at the edge-point of each surface which is the closest to the surface.

smoothing of the edge would increase this risk. An increased hull with smooth boundaries would remove this problem, but add unnecessary conservatism around the edge where certain free parts of the space can not be reached by the autonomous agent.

Moreover, a high gradient surface used with the obstacle avoidance algorithm we offered in [32] leads to fast change of flow. Even though the trajectories are smooth the curvature of the flow can be high which might be undesired as it comes with fast accelerations. This may lead to dangerous behavior in the presence of humans or simply exceed the robot's torque limits. Instead, we propose an algorithm to avoid obstacles with non-smooth surfaces without smoothing the boundary.

A polygonal obstacle consists of $i = 1..N^s$ individually smooth surface planes and of a set of continuous points which form a star shape in $d-1$, as given in (6), such that:

$$\mathcal{S}_i = \{\xi, \hat{\xi} \in \mathcal{B}, \exists \mathbf{n} : \mathbf{n}^T(\xi - \hat{\xi}) = 0\} \quad (23)$$

A. Pseudo Normal Vector

The normal to the surface of the obstacle is not defined continuously. Hence, the modulation with the basis matrix from (16) is not smoothly defined and the modulated system results in a non-continuous flow. For this reason, the basis matrix is redefined for non-smooth surfaces as

$$\mathbf{E}(\xi) = [\mathbf{r}(\xi) \hat{\mathbf{e}}_1(\xi) \dots \hat{\mathbf{e}}_{d-1}(\xi)] \quad (24)$$

with $\hat{\mathbf{e}}_i(\xi)$ for $i = 1..d-1$ begin the orthonormal basis to the pseudo normal $\hat{\mathbf{n}}(\xi)$ which is continuously defined in free space.

The pseudo normal is evaluated as the directional mean (Sec. II-B) of all normal vectors $\mathbf{n}_i(\xi)$ of the individual surfaces. The orthonormal transformation matrix \mathbf{R}^0 is created based on the reference vector, i.e. $\mathbf{r}^o = \mathbf{r}(\xi)$. The weights are chosen such that the pseudo norm is equal to the actual norm on the surface of the obstacle, while away

the obstacle the pseudo normal needs to be smoothly defined. Here we chose it based on the angle distance to the surface with respect to a edge point .

At first the vector from the closest surface point \mathbf{p}_i^s (Fig. 6) to the agent's state is created:

$$\mathbf{v}_i^{\zeta}(\xi) = \xi - \mathbf{p}_i^s \quad \text{with} \quad \mathbf{p}_i^s = \underset{\chi \in \mathcal{E}_i}{\operatorname{argmin}} \|\xi - \chi\| \quad (25)$$

the point being at the edge of a source \mathcal{E}_i . This vector is projected onto the surface plane:

$$\hat{\mathbf{e}}_i(\xi) = \left(\mathbf{v}_i^{\zeta}(\xi) - \langle \mathbf{n}_i(\xi), \mathbf{v}_i^{\zeta}(\xi) \rangle \mathbf{n}_i(\xi) \right) \operatorname{sign} \langle \mathbf{v}_i^{\zeta}(\xi), \xi - \xi_i^{r,s} \rangle$$

The angle to the plane (Fig. 6) in the range $[0, \pi]$ is evaluated as:

$$\phi_i^w(\xi) = \arccos \frac{\langle \hat{\mathbf{e}}_i(\xi), \mathbf{v}_i^{\zeta}(\xi) \rangle}{\|\hat{\mathbf{e}}_i(\xi)\| \|\mathbf{v}_i^{\zeta}(\xi)\|} \operatorname{sign} \langle \mathbf{n}_i(\xi), \mathbf{v}_i^{\zeta}(\xi) \rangle \quad (26)$$

Which leads to the non-normalized edge weight is evaluated as:

$$\tilde{w}_i^s(\xi) = \begin{cases} \left(\frac{\phi_i^{w,max}}{\phi_i^w(\xi)} \right)^p - 1 & \text{if } \phi_i^w(\xi) \in]0, \phi_i^{w,max}] \\ 0 & \text{if } \phi_i^w(\xi) \notin [0, \phi_i^{w,max}] \end{cases} \quad (27)$$

with the limit angle $\phi_i^{w,max} \leq \pi$ and the weight power $p \in \mathbb{R}$. We choose $\phi_i^{w,max} = \pi$ and $p = 3$. In the case of $\phi_i^w(\xi) = 0$, which implies $\xi \in \mathcal{S}_i$ the weight results from (28) in one.

The final step is the normalization:

$$w_i^s(\xi) = \begin{cases} \tilde{w}_i^s(\xi) / \sum_j \tilde{w}_j^s(\xi) & \text{if } \xi \in \mathbb{R}^d \setminus \mathcal{S}_i \\ 1 & \text{otherwise} \end{cases} \quad (28)$$

B. Inverted Obstacles

This continuous pseudo normal and hence the basis matrix $\mathbf{E}(\xi)$ for non-smooth surfaces given in (24) is not uniquely a function of the direction. In order to evaluate the pseudo normal for an Inverted obstacle, current robot state ξ is mirrored along the reference direction $\mathbf{r}(\xi) = \xi - \xi^r$ to a position ξ^{mir} on the other side of the boundary: (4) as:

$$\xi^{mir} = \Gamma(\xi)^2 (\xi - \xi^r) + \xi^r \quad (29)$$

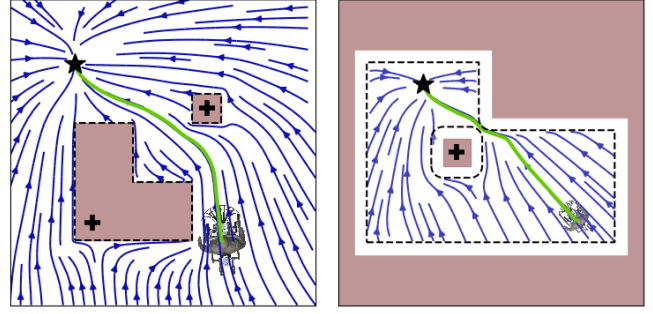
The mirrored position allows to evaluate the distance function as described in Sec. V-A. Further, the inverted obstacle is treated as described in Sec. IV. This allows to avoid obstacles in Fig. 7.

Theorem 3 Consider a polygon composed of N^s surfaces as given in (23) or alternatively a inverted polygon as described Sec. V-B. Any trajectory $\{\xi\}_t$, that starts in free space, i.e. $\Gamma(\{\xi\}_0) > 1$ and evolves on a smooth path according to (15), will never reach the surface, i.e. $\Gamma(\{\xi\}_t) > 1, t = 0..∞$ and converge towards an attractor in free space, i.e. $\lim_{t \rightarrow \infty} \xi \rightarrow \xi^a \in \mathcal{F}$. **Proof:** see Appendix C.

VI. DYNAMIC ENVIRONMENTS

In changing environments (moving or deforming obstacles) the system is modulated with respect to a local, relative velocity such as:

$$\dot{\xi} = \mathbf{M}(\xi) \left(\mathbf{f}(\xi) - \dot{\xi}_o \right) + \dot{\xi}_o \quad (30)$$



(a) Non-smooth obstacles (b) Non-smooth boundaries
Fig. 7: Non-smooth Inverted obstacles representing rooms or boundary conditions.

The relative velocity consists of the obstacle velocity $\dot{\xi}_v$ and the part from the deforming obstacle $\dot{\xi}_d$:

$$\dot{\xi}_o = \dot{\xi}_v + \dot{\xi}_d \quad (31)$$

A. Moving Obstacles

For moving obstacles the modulation is performed in the obstacle reference frame, and then transformed to the inertial frame [33]:

$$\text{with } \dot{\xi}_v = \dot{\xi}_v^{L,o} + \dot{\xi}_v^{R,o} \times \tilde{\xi}_v \quad (32)$$

with linear and angular velocity of the obstacle with respect to its center point $\dot{\xi}_v^{L,o}$ and $\dot{\xi}_v^{R,o}$, respectively and the relative position $\tilde{\xi} = \xi - \xi^c$. Avoiding moving obstacles is not a pure modulation of the DS in form of a matrix multiplication anymore, hence topographically critical points, including the attractor, can be displaced.

B. Deforming Obstacle

The environment of the robot can in many cases have not only moving obstacles, but they may also be deformable, e.g. changing self-collision limits in joint space, moving body for a surgery robot. The deformation can also be the result of estimating an obstacle surface and updating this estimate in real time.

We introduce a factor related to the surface deformation:

$$\dot{\xi}_d = \dot{\xi}_d^{L,o} + \dot{\xi}_d^{R,o} \times \tilde{\xi}_d \quad (33)$$

Where the linear and angular velocity are at the surface position in reference direction.

If the expansion is now as a model-parameter of the obstacle (e.g. expanding heart for a surgery setup) this can be evaluated from the model. In environments which are constructed from the surrounding this With moving obstacle and moving obstacle this can be complex to evaluate.

For a circular object, we have:

$$\dot{\xi}_d = \dot{\xi}_d^{L,o} = \begin{cases} \dot{r} \mathbf{n}(\xi) & \dot{r} > 0 \\ 0 & \text{otherwise} \end{cases} \quad (34)$$

where \dot{r} is the rate of change in time of the circle radius.

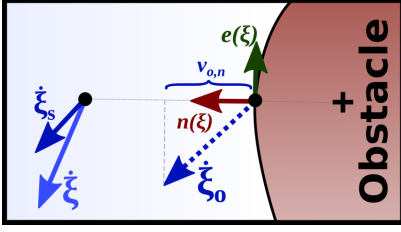


Fig. 8: In order to comply with a velocity limit of the robot while avoiding a collision with an obstacle of velocity ξ_o , the modulated velocity ξ might be stretched only in tangent direction to obtain the save velocity command \dot{x}_s .

C. Impenetrability with Respect to Maximum Velocity

In critical situations, i.e. when the agent is close to an obstacle, the agent needs to move away from the obstacle. The relative velocity of the surface must hence point towards the agent. When projected onto the normal direction $v_{o,e}$, this relative velocity is therefore limited to:

$$v_{o,n} := \langle \xi_o, \mathbf{n}(\xi) \rangle < v_{max} \quad \forall \Gamma(\xi) \rightarrow 1 \quad (35)$$

where v_{max} is the maximum velocity of the agent (see Fig. 8). If the agent is close to the obstacle's surface, its final velocity ξ_s is evaluated as:

$$\xi_s = \begin{cases} v_{o,n} \mathbf{n}(\xi) + \sqrt{v_{max}^2 - v_{o,n}^2} \mathbf{e}(\xi) & \text{if } \langle \xi, \mathbf{n}(\xi) \rangle \frac{v_{max}}{\|\xi\|} < v_{o,n} \\ v_{max} / \|\xi\| \xi & \text{else if } \|\xi\| > v_{max} \\ \xi & \text{otherwise} \end{cases} \quad (36)$$

The evaluation is based on the obstacle's surface velocity ξ_o and the modulated velocity in dynamic environments ξ as given in (30).

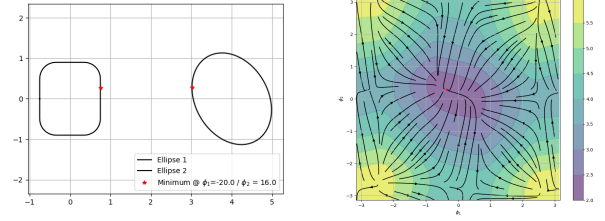
Theorem 4 Consider the dynamic environment including one obstacle which has a surface velocity ξ_o , including by the obstacle moving or expanding, given as (31). An agent is moving in this space and has a maximum velocity of v_{max} , further the obstacle's surface velocity is limited by (35). The agent which starts in free space, i.e. $\Gamma(\{\xi\}_0) > 1$ and moves according to (36), will stay in free space for infinite time, i.e. $\Gamma(\{\xi\}_t) > 1, t = 0..∞$. **Proof:** see Appendix D.

VII. DYNAMIC REFERENCE POINTS PLACEMENT

The reference point plays an important role in the behavior of the algorithm. In a dynamic environment it has to be evaluated and adapted in real time to allow for the robot to converge to the attractor. We propose an algorithm which finds the closest point for each pair of obstacles separately. This is then expanded to find the optimal position of more convex environments. The algorithm focuses on convex obstacles. More star-shapes can be formed through the combination of convex obstacles.

A. Pairwise Closest Distance in Direction Space

First step is to find the closest distance between two (convex) obstacles. This is done by moving along the surface



(a) Minimum Distance

(b) Value Function

Fig. 9: The minimum distance problem for a squared object (with boundary) and an ellipsoid. The boundary-reference-point which corresponds to the closes point is marked in red (a) and the corresponding gradient descent problem in direction space (b).

of the obstacle in direction space. The optimization problem is such that:

$$\min \mathbf{f}_b(\xi) = \min_{\|\mathbf{v}_1\|, \|\mathbf{v}_2\| \leq \pi/2} \|\mathbf{s}_1(\mathbf{v}_1) - \mathbf{s}_2(\mathbf{v}_2)\| \quad (37)$$

where the $\mathbf{s}_i(\mathbf{v}_i)$ denotes the surface point in direction \mathbf{v}_i . The direction space of each obstacle is created such that the null-direction points towards the other obstacles center. With the gradient step being defined as:

$$\mathbf{v}^{k+1} = \mathbf{v}^k + \alpha_{b,k} \nabla \mathbf{f}(\mathbf{v}^k) \quad (38)$$

with $\mathbf{v} = [\mathbf{v}_1^T \ \mathbf{v}_2^T]^T$.

The direction of the null-space and initial direction as described above leads to a non-convex optimization problem in direction space, where the local minima of (37) is the local minimum (see Fig. 9 for an example).

1) *Inverted Obstacles:* In many scenarios, the obstacles can intersect with the enclosing space boundary. This case requires the placement such that we have still full convergence. We will assume that the curvature of the obstacle c_o is larger than the curvature of the boundary c_b at any position:

$$c_o(\xi_1) < c_b(\xi_2) \quad \forall \xi_1, \xi_2 \quad (39)$$

The local curvature is given as:

$$c_{(\cdot)} = \lim_{\mathbf{d}\xi \rightarrow 0} \frac{R(\xi) - R(\xi + \mathbf{d}\xi)}{\mathbf{d}\xi} \quad \forall \xi \in \mathcal{X}^b, \mathbf{d}\xi^T \mathbf{n}(\xi) = 0$$

Note for non-circular obstacles condition (39) might locally not hold true. Especially if the space contains polygon obstacles with local flat regions ($c = 0$). This can lead to locally non-optimal solution in special cases (e.g. the obstacle is close to the boundary's edge, where the curvature approaches infinity). In general scenarios, the obtained solution show the desired output.

B. Intersecting Obstacle Descent

Two intersecting obstacles have one common reference point. It is additionally not on the surface anymore. The simplification of the space is therefore not an advantage anymore. In the case, that the surface reference point is found in the other obstacle, the optimization problem is changed to find an optimal common point:

$$\min \mathbf{f}_i(\xi) = \min_{\xi \in \mathcal{X}_1^b \cap \mathcal{X}_2^b} \frac{1}{1 - \Gamma_1(\xi)} + \frac{1}{1 - \Gamma_2(\xi)} \quad (40)$$

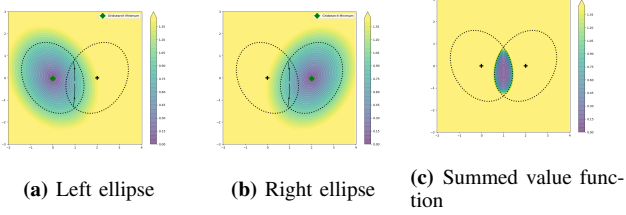


Fig. 10: The sum of the value functions from (a) and (b) allows to find an optimal common point of the two obstacles (c)

A gradient descent step is performed in direction space:

$$\xi^{k+1} = \xi^k + \alpha_{i,k} \nabla \mathbf{f}_i(\xi) \quad (41)$$

The step size can be optimized based on the gradient. The optimization problem is convex and point starting within the intersection region will stay inside due to the infinite repulsion at the boundary as $\Gamma \rightarrow 1$. The value function of two ellipse obstacles can be found in Fig. 10.

C. Reference Point Evaluation

At each time step, the gradient descent is performed to evaluate two boundary-reference-point for each pair of obstacles (within the margin region). This point is used as initialization at the next time step. Since the obstacles can only move a small amount at each time step, the needed gradient descent to the global minimum is small. Additionally, as the update rate increased, the movement distance at each time step decreases. The reference point is evaluated each time step as a weighted sum of all boundary reference point of an obstacle.

D. Dynamic Extension of Hull

In many scenarios the obstacles can form clusters which cannot be approximated by star-shapes anymore. We propose the dynamic extension of the surfaces. Since the algorithm can work with deforming hulls (Sec. VI-B) the shape of the obstacle can be extended to meet the obstacle avoidance requirements.

The reference point is expanded such that each obstacle forms a convex obstacle with it. This can be done by extending the hull with a cone that is tangent to the obstacles surface, but has the tip at the reference point (Fig. 11). Note that the reference point is placed for a globally optimal solution. Future work, we will try to extend this work to allow the reference point to adapt locally.

E. Mixed Scenarios

Real world implementation have often a mix of obstacles and boundaries moving. Often scenarios can occur where the obstacles intersect with the boundaries (see Fig. 12). The reference point of the boundary obstacle only be displaced in a limited region. Furthermore, moving it has little influence to the convergence of the obstacles. The reference point of the obstacles which are intersecting with the wall can be placed inside the wall, i.e. $\Gamma_b(\xi_{ref}) < 1$. This enforces that all trajectories avoid the obstacles around the same side which also the boundary enforces them and leads to full avoidance

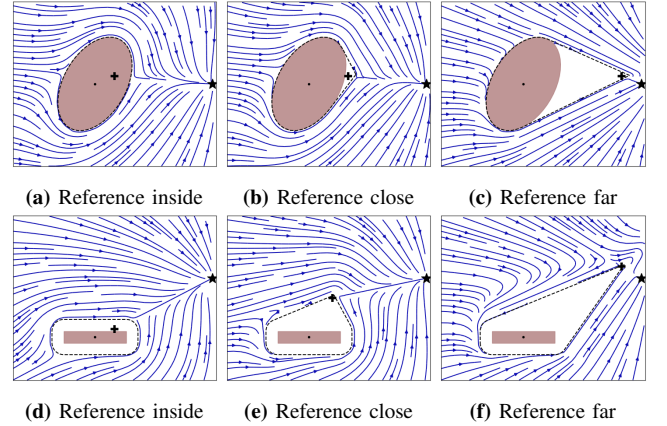


Fig. 11: Dynamic extension of the hull for an ellipsoid object without margin (a)-(c) and a non-smooth polygon object with constant margin in all directions (d)-(e).

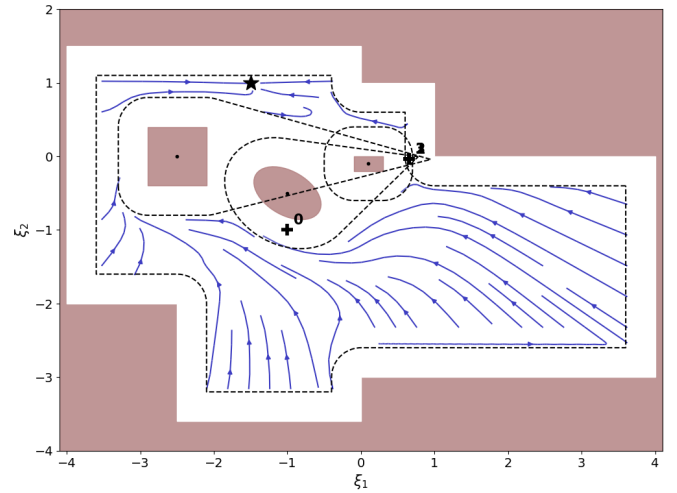


Fig. 12: Full convergence towards the attractor in an environment of three obstacles intersecting with the boundary.

of the whole DS. This is true for a boundary-obstacle with a positive (local) curvature, i.e.:

$$c_b(\xi) > 0 \quad \forall \xi \quad (42)$$

In such a scenario, there is full convergence of the dynamical system towards the attractor.

VIII. COMPARISON ALGORITHMS

The method for the modulation algorithm in dynamic environments as presented in this paper (referred as *Dynamic* during this section). It is compared to [34], which uses modulation matrix which uses an orthogonal decomposition matrix $\mathbf{E}(\xi)$ (referred as *Orthogonal*) and the potential field algorithm and to [14], a potential field algorithm (referred as *Repulsion*). The comparison algorithms have been chosen on the base, that it had to be a local-collision avoidance algorithm, and able to handle external hulls.

The comparison is done in an environment as Fig. 13. The two ellipse shaped obstacle are randomly changing shape during the motion, and move in a random walk manner. The combined maximum expansion velocity and obstacle velocity is lower than the maximum speed of the three agents of $1m/s$. The *Dynamic* algorithm is observed to have the most convergences (Tab. I). This is the result of the fact, that it has

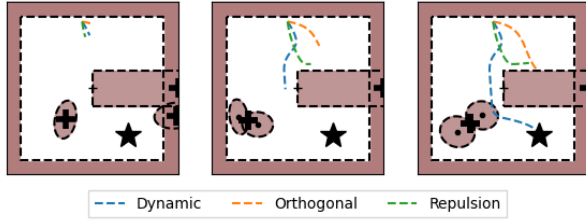


Fig. 13: An example of a simulation with the three different algorithms. Full convergence is observed due to the additional knowledge about the environment for the algorithm presented in this work.

with the knowledge of the reference point a better knowledge of the environment. The *Repulsion* has a preferable behavior on avoiding collisions. This is the result of a conservative behavior around obstacles (moving far away and only approaching them slowly). This has an effect on the distance, but especially the time needed to reach a goal (Tab. II). The mean of the velocity is lower for the *Dynamic* algorithm. This is expected to be the result of the reduced influence behind the obstacles (see Sec. III-2). The variance of the velocity is similar for the three algorithms.

IX. EMPIRICAL VALIDATION

The empirical validation is performed first in simulation and then on a real robot platform. We use the mobile robot QOLO [35], see Fig. 14. The mobile platform QOLO, a semi-autonomous wheel chair, is designed to navigate in pedestrian environments and indoors. This platform is hence ideally suited to test our algorithm’s ability to avoid rapidly many moving obstacles (pedestrians) and non-convex obstacles (walls, indoor furniture) containing sharp edges (tables, shelf). In all our experiments, we assume that QOLO has received a high-level command from its user to set the desired end-goal, i.e. the attractor x^* of our nominal DS. A video of the experiments is available at ².

A. Static Environment

We task QOLO to navigate in an office-like environment. The room is a square (5m x 5m), modelled as a boundary obstacle with 4 walls including the closed door. Further, there are two clusters of tables which disturb the path of the robot

²www.To Be Uploaded.com

	Converged	Collided	Minimum
Dynamic	77%	23%	0%
Orthogonal	20%	23%	57%
Repulsion	39%	1%	60%

TABLE I: The percentage out of 300 trials of success full runs, once where the trajectory collided with an obstacle and runs which ended up in a local minimum.

	d [m]	t [s]	\bar{v} [m/s]	σ_v [m/s]
Dynamic	9.69 ± 1.19	1.03 ± 0.13	0.61 ± 0.05	0.34 ± 0.02
Orthogonal	10.06 ± 1.53	1.17 ± 0.21	0.55 ± 0.05	0.34 ± 0.02
Repulsion	9.8 ± 1.29	1.39 ± 0.2	0.46 ± 0.03	0.21 ± 0.02

TABLE II: The mean and the standard deviation (after the ±) are compared for the three algorithms from the 54 trials where all three agents converged. The metrics of distance (d), duration of the run (t), the mean velocity (\bar{v}) and the standard deviation of the velocity (σ_v) are listed.

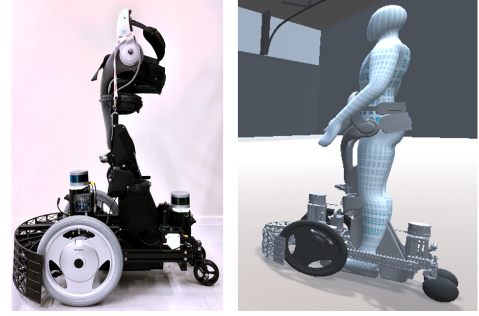


Fig. 14: A picture of the semi-autonomous wheelchair real (left) and the simulated with a person operating it (right).

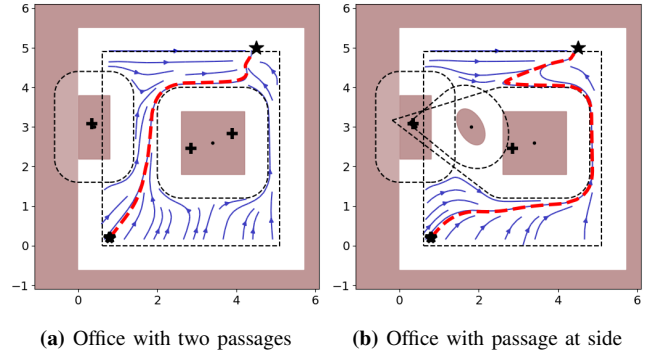


Fig. 15: Two static office environments including two tables in a rectangular room. There exist two passages (a), which is blocked by a static person in (b). The reference point (black cross) guide the flow to the attractor (black star). The experimental path is displayed in red.

(one at the side and one at the center of the room). The robot starts from one of the wall (the simulates the robot entering the room) and is tasked to reach the opposite diagonal position (illustrated with a cross). All objects are static and known, the localization is performed using SLAM algorithm. The robot gets an input dynamical system which is further modulated as described in this paper. We observe following two scenarios: A) QOLO is in the room, and there are two possible paths to go around the center table. The dynamical systems splits freely.

The robot is able to find a path in the two scenarios, even without global planning but only local adaptation. The table in the middle as in Fig. 15a, the dynamical system is split around the center table. The robot chooses it’s preferred trajectory on the go.

B) Additionally there is a (static) person in the room, which blocks the center passage.

Due to the optimization of the reference points, at the common placement at the wall, the robot finds its way around. It is to notice, that due to the fact that the modulated flow is tangent on the surface, we can observe behavior in front of and behind the obstacles which is not optimal.

B. Dense Crowd (Simulation)

The robot is navigating in a corridor jointly with in a dense, simulated crowd. The motion of the crowd is created according to [36]. To navigate successfully, the robot must avoid all pedestrians and the walls. A crowd of 200 people is moving along (same and opposite direction as the robot) in a 6 meter wide corridor.



Fig. 16: QOLO moving in a crowd.

QOLO is tasked to travel from one end of the corridor to the other end, where we set the attractor of the nominal DS. All pedestrians are modeled as circular obstacles with radius of 0.6 meters (Fig. 17a).

At each timestep, the problem is reduced to avoiding a subset of the pedestrians. Indeed, due to the density of the crowd, the robot could realistically perceive only a subset of the pedestrians in real-time. We, thus, set that only a set number of closest people ($n_c = 10$) are perceived. We additionally introduce a circular wall. All remaining obstacles are hidden behind this virtual wall. The center of the circular wall $\xi_{c,w}$ is displacement from the position of the robot ξ_0 based on the remaining obstacles:

$$\xi_{c,w} = \xi_0 + \sum_{i=n_c+1}^{N_{obs}} \frac{\xi_{c,i} - \xi_0}{\|\xi_{c,i} - \xi_0\|} e^{-\left(\|\xi_{c,i} - \xi_0\| - r_p - m_q\right)} \quad (43)$$

where i is iterating over the ordered list based on the distance. The displacement factor is with respect to the radius of a each pedestrian ($r_p = 0.6m$) and the robot radius m_q .

Note, that for a real implementation sensory distance measurements in the horizontal plane can be used to create the circular boundary.

The radius of the hull is chosen such that the next closest obstacle $n_c + 1$ is fully within the hull. The resulting environment has a hull with changing center-position and radius (Fig. 17). The reduction of the environment to only sphere obstacles allows to speed up the computational time, since there exist a solution for the closest distance between two spheres. This allowed to evaluate the local world at a frequency of over 1000 Hz, even with eleven obstacles in close proximity (including the wall). While the agent remains far away from the wall, it is still crucial to guide the robot around local crowds. This is done as the reference point is placed at the wall, if a crowd-cluster is touching it (see small cluster at the bottom in Fig. 17b). Further, fast contraction of the boundary (in case of many people in the surrounding) forces the obstacle to stay away from surrounding obstacles.

1) *Quantitative Analysis:* We evaluate the effect of the crowd size on the time it takes for the robot to travel through the corridor. The crowd's motion is generated through a realistic simulator created by [36]. Each crowd flow is meant to move from one end of the corridor to the other end. The crowd has an average velocity of $1m/s$. When all agents have the same goal, that is when they move towards the same corridor's end, the crowd tends to structure into a uniform flow. We run our simulation in such a steady-state crowd-flow, with the QOLO-agent either integrating and moving in the same direction, or moving into the opposite direction of

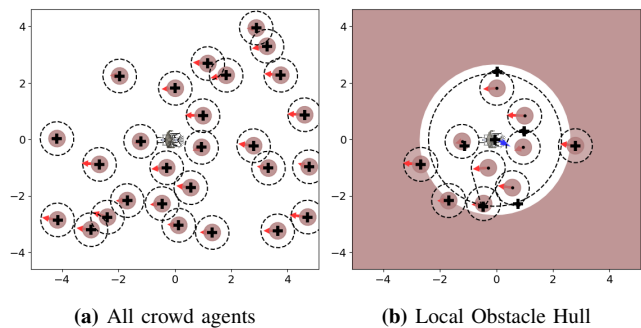


Fig. 17: The environments with many agents (left) is reduced to a scenario with 10 obstacles and an enclosing hull (right).

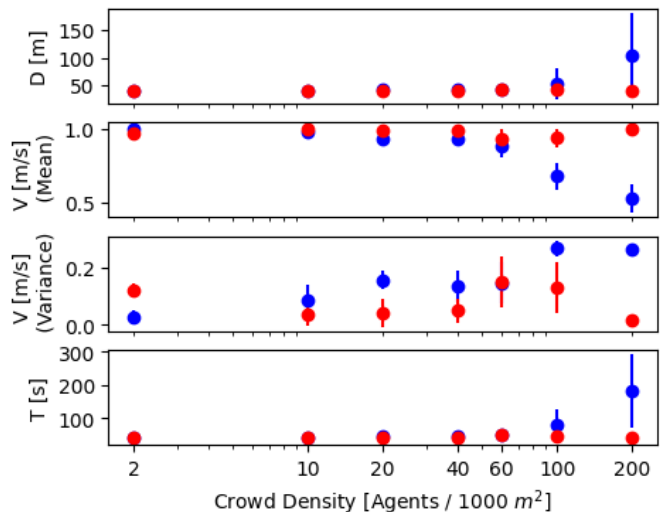


Fig. 18: The QOLO agent is moving in parallel (red) and opposite direction (blue) to the crowd. When the robot moves with the crowd, the density of the crowd has negligible effect. When the robot moves in opposite direction, the denser the crowd, the larger the cumulative distance (D) and mean velocity (V) as well as time (T) needed to reach the end of the corridor (T). The standard deviation of the velocity (V Std.) increases in counter flow for more dense crowds.

the crowd. The robot has a desired velocity of $1m/s$.

We assess the time, speed and distance travelled by the robot when moving with and opposite to the flow, see Fig. 18. When moving with the flow (i.e. In parallel-flow), the crowd has no significant effect on the distance travelled by the agent and its velocity. When moving against the crowd (counter-flow), a decrease of the robot's velocity can be observed for crowds denser than 20 agents per 1000 square-meters. (The effect on the crowd was observed, since the effect is small as only a single robot moving against a large crowd.) The distance travelled increases significantly for densities above 100 agents per 1000 square-meters. As a result, the time mean time needed to reach the goal more than doubles for a crowd-size of hundred people.

In counter flow scenarios, the standard deviation of the flow increases. This results from situations where the robot has to slow down or stop in order to avoid the upcoming agents.

C. Proof of concept: Outdoor Environment

A qualitative proof of concept was performed in an outdoor environment. We brought the QOLO robot in the center of

Lausanne, Switzerland city³. The robot was tasked to travel back and forth across a small market place (Fig. 19). The location is restricted to pedestrians only, and a total of six streets meet at the crossing. This results in a large diversity in both the pedestrian’s velocities and directions of movement. The path is about 20 meters long and the robot’s controller is initialized with a linear DS to reach a goal 20 meters away from the onset position. Pedestrians are detected with a camera and LIDAR-based tracker published in [37] as can be seen in Fig. 20. Recordings were taken on Saturday morning when the market is running full blow and the crowd was the densest. The dynamical system is transferred into the controller of the non-holonomic, by placing the evaluation point 0.53 m in front of the center of the wheel-axes (in the reference frame of the robot). The dynamical system is evaluated at this point, and the linear velocity is the part parallel in moving direction, the angular velocity is perpendicular. The geometry of QOLO is taken into account, by placing a margin around each pedestrian of with 0.5 m. The different method from the simulator was chosen in order to reduce the angular acceleration. A total of five runs were executed with the detector. The robot reached its goal without intervention of the drive. The driver reported that in some cases the robot had *high angular acceleration*.

Post-hoc analysis of the video recordings revealed that the crowd density varied with a mean between 5 and 7.5 people per square meter (Fig. 21). The agent completed the runs within 115 and 150 seconds. No correlation was observed between the density of the crowd and the time taken to reach the goal. This is to be expected, since many additional factors influence the duration of the run, such as distribution and the motion of the crowd.

We see this as a successful proof-of-concept test of the obstacle avoidance in real crowd scenarios. Compared to the stream-line simulation the crowd motion was more complex, as people would come from all directions and would not group in steady flow. Moreover, the crowd included a large diversity in the type of pedestrians, from families with small children to elders.

X. DISCUSSION AND FUTURE WORK

The algorithms have theoretical proof and possible application in higher dimensional space. Current application has been focusing on the avoidance in two dimensional application such as navigation of mobile robots. We plan to apply the algorithm further on in three dimensional task space, but also use it for control in joint space. The development of faster transformation such as [38] will make such algorithms more interesting. Many sampling methods are not easily salable to higher dimensions, due to increasing computational cost. We expect the present method to be of advantage there.

The concept of dividing dynamical systems into direction and magnitude and the presented method summing vectors

³Appropriate ethics and safety approval were obtained from the EPFL Ethics board and Policy of Lausanne city. A driver was on-board of the robot. He could start and stop the robot by pressing on the on-board button, as required for pedestrians’ safety. A second experimenter was watching the scene and verified the output of the Lidar-vision tracker on a separate laptop. This was necessary if needed to guarantee proper safety, in case the detector/tracker dis-functioned.



Fig. 19: The desired path of the robot in the outdoor environment is the direct line from the initial position of the robot (right) to the target position in the left.

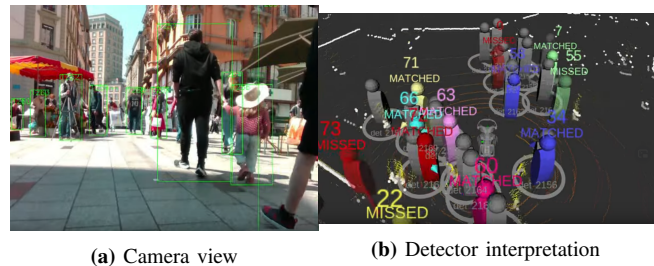


Fig. 20: The camera (a) and the LIDAR of the robot are interpreted by the detector (b), which is used for the obstacle avoidance algorithm.

to avoid local minima has been used throughout the paper. It was used in three areas: (1) creating a smooth pseudo-normal for polygon obstacles and walls, and from that a smooth flow in their presence, (2) it allowed the summation of the flow created by several obstacles without creating local minima and (3) to solve the optimisation problem to find the closest distance for pairs of obstacles. We plan to explore the direction space further in motion control, but also learning by demonstration. Further having a unified description will allow to extend obstacle avoidance to initially nonlinear motion.

Since many human-made environments contain non-smooth surfaces (e.g. tables, corners of rooms), the solution for providing a smooth flow without creating an additional hull around is of great value for practical implementations.

The inverted obstacle has proposed itself as a great representation for limitations of mobile robots, such as walls of a room or the local window in dense crowd navigation. We will further explore these boundaries to control constraints similar to control barrier functions (CFD). Recent development have used such control barrier function in the context of safe learning by demonstration [39], [40] or reinforcement learning [41]. Other than existing methods, we propose closed form solution for star-shaped barriers. Future work could include

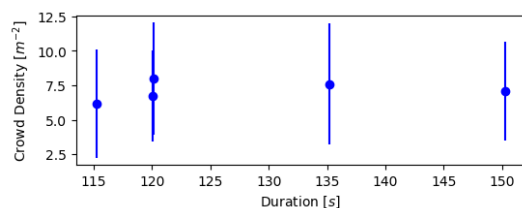


Fig. 21: The crowd-density is highly varying during the five successful runs.

the application of the presented algorithm as barrier function and further extend it to the velocity space.

The algorithm has been successfully moved on a non-holonomic robot in a static indoor environment and a dynamic outdoor crowd. The robot's behavior could however be improved in three areas:

- **Low-level controller:** The low-level controller displaced the evaluation of the DS from the center of the robot. This resulted into an increased (conservative margin around the robot). The design of the controller could be improved by taking into the consideration the local evolution of the DS.
- **Environment Recognition:** The update rate of the tracker has been around 5 Hz. The algorithm is running at a frequency between 50 Hz to 100 Hz, and hence often evaluates with old environment information. An intermediate predictor/estimator of how the crowds move in-between could help bridge this gap.
- **High-level Planning:** The combination of the fast obstacle avoidance controller with a slower, planning algorithms could allow to handle more complex environments, i.e. including the avoidance of surrounding (non-starshaped) environments.

XI. CONCLUSION

A dynamical system based algorithm for local navigation under convergence constraint is presented in this paper.

The present method provides a good solution for local crowd navigation. It ensures certain convergence constraint to not only safely navigate, but also reach goal in local scenarios.

The advantage of presented concepts come from the low complexity and speed of the algorithm. This allows it to extend to scale to higher dimensions and transfer to other scenarios.

XII. ACKNOWLEDGEMENT

We would like to thank the support of Diego Felipe Paez Granados and David Gonon for the running of the experiments. Their effort and insight has helped a lot in the qualitative analysis of these results.

APPENDIX

A. Proof of Theorem 1

We show the existence of a *bijection* in three steps: (1) showing that transformation and reconstruction function are the inverse function of each other, (2) any unit vector is transformed to the vector space domain, and (3) any vector space vector is reconstructed to a unit vector.

1) *Inverse Function:* For the transformation and reconstruction functions to generate a bijection, applying one after the other result in the initial value.

Let us apply the transformation function from (11) and the reconstruction function (13) to any unit vector (except $\pm \mathbf{r}^0$, as they will be treated separately bellow).

$$\kappa^1(r^0) = \arccos(\langle \mathbf{r}^0, \mathbf{v}^1 \rangle) \frac{(\hat{\mathbf{R}}^0)^T \mathbf{v}^1}{\|(\hat{\mathbf{R}}^0)^T \mathbf{v}^1\|} \quad (44)$$

with $\hat{\mathbf{R}}^0$ being the partial matrix of \mathbf{R}^0 without the first column. We apply it to a single vector (i.e. $N^v = 1$), hence the corresponding weight is $w^i = 1$, as a result we have $\bar{\kappa} = \kappa^1$. The reconstruction follows as:

$$\begin{aligned} \bar{\mathbf{v}} &= \mathbf{R}^0 \left[\cos \|\bar{\kappa}\| \quad \sin \|\bar{\kappa}\| \frac{\bar{\kappa}}{\|\bar{\kappa}\|} \right]^T \\ &= \mathbf{r}^0 \cos(\arccos(\langle \mathbf{r}^0, \mathbf{v}^1 \rangle)) + \frac{\hat{\mathbf{R}}^0 \sin(\arccos(\langle \mathbf{r}^0, \mathbf{v}^1 \rangle)) (\hat{\mathbf{R}}^0)^T \mathbf{v}^1}{\|(\hat{\mathbf{R}}^0)^T \mathbf{v}^1\|} \\ &= \langle (\mathbf{r}^0)^T, \mathbf{v}^1 \rangle \mathbf{r}^0 + \hat{\mathbf{R}}^0 (\hat{\mathbf{R}}^0)^T \mathbf{v}^1 = \mathbf{v}^1 \end{aligned}$$

because of $\sin(\arccos(\langle \mathbf{r}^0, \mathbf{v}^1 \rangle)) = \sqrt{1 - \langle (\mathbf{r}^0)^T, \mathbf{v}^1 \rangle^2} = \|(\hat{\mathbf{R}}^0)^T \mathbf{v}^1\|$. This follows from the fact $\| \text{matr} \mathbf{R}^0 \mathbf{v}^1 \| = 1$ (rotated unit vector).

The special case of \mathbf{r}^0 is projected on the trivial vector $\kappa = \mathbf{0}$ (11). Finally it is reconstructed (13 as \mathbf{r}^0).

2) *Transformation Domain:* Any possible direction vector is transformed with (11) the set of direction space \mathcal{K}^π given in (8).

The limitation of the set is by definition in (11) the magnitude of κ . Using (10), the maximum of the magnitude can be evaluated:

$$\|\kappa\| = \arccos(\hat{\mathbf{v}}_1^i) = \arccos(\langle (\mathbf{r}^0)^T, \mathbf{v}^i \rangle) \begin{cases} = \pi & \text{if } \mathbf{v}^i = -\mathbf{r}^0 \\ < \pi & \text{otherwise} \end{cases}$$

3) *Reconstruction Domain:* Any vector $\kappa \in \mathcal{K}^\pi$ reconstructed with (13) is in the set of possible unit vectors.

From (13) we can get that $\|\bar{\mathbf{v}}\|^2 = 1$. Hence, we get any unit directional vector but $-\mathbf{r}^0$, since $\cos \|\bar{\kappa}\| > -1$, since $\|\bar{\kappa}\| < \pi$ by definition of the set \mathcal{K}^π .

B. Proof of Theorem 2

1) *Applicability of General Proofs:* In [32] a corresponding theorem has been proven for star-shaped obstacles. The proof was developed based on the distance function $\Gamma(\xi)$ the basis matrix. Due to inverting the distance function for enclosing wall obstacles and a continuous definition of the modulation, the proof of star-shaped obstacles applies to the case of enclosing walls.

2) *Discontinuity Across ξ^r :* In Sec. IV-A the Inverted distance function $\Gamma^w(\xi)$ was not defined at the reference point, as it reaches an infinite value. The continuous definition for the eigenvalue is a unit value, i.e. $\lambda_e(\xi^r) = \lambda_r(\xi^r) = 1$, it follows that the diagonal matrix is equal to the identity matrix $D(\xi^r) = I$. From this we get for the modulated dynamical system 15:

$$\xi = \xi^r \rightarrow \dot{\xi} = \mathbf{E} \mathbf{D} \mathbf{E}^{-1} \mathbf{f}(\xi^r) = \mathbf{E} \mathbf{I} \mathbf{E}^{-1} \mathbf{f}(\xi^r) = \mathbf{f}(\xi^r) \quad (45)$$

i.e. no modulation of the initial DS. In fact, this is equivalent to the case far away for a classical obstacle with $\lim_{\|\xi - \xi^r\| \rightarrow \infty} \Gamma^o(\xi) \rightarrow \infty$.

Even though the basis matrix $\mathbf{E}(\xi)$ is not defined at ξ^r , the DS is continuously defined across this point since the modulation has no effect.

Note that the trajectory which goes through the reference point ξ^r of the inverted obstacle is corresponding to the trajectory which gets stuck in a saddle point for the normal obstacle. As a result, there is full convergence for the inverted obstacles.

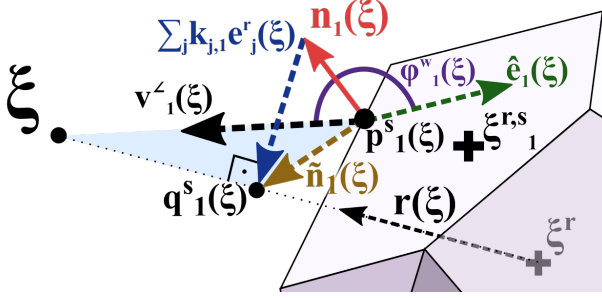


Fig. 22: Visualization of variables used for the weighted directional mean.

C. Proof of Theorem 3

We show first that the modulation has full rank and hence that the dynamics does not vanish outside the attractor and that it is smooth.

1) *Full Rank*: The basis matrix from (24) has full rank everywhere outside of the obstacle, if the following condition holds:

$$\arccos\langle \mathbf{r}(\xi), \hat{\mathbf{n}}(\xi) \rangle < \pi/2 \quad (46)$$

The angle between the normal to each surface i , $\mathbf{n}^i(\xi)$ and the reference direction $\mathbf{r}(\xi)$ can be evaluated by defining an vector $\hat{\mathbf{n}}^i(\xi) = \mathbf{n}^i(\xi) + \sum_{j=1}^{d-1} k_j^e \mathbf{e}_j(\xi)$ with $\langle \mathbf{e}_j(\xi), \mathbf{r}(\xi) \rangle = 0$, $k_j^e \in \mathbb{R}$ such that $\mathbf{p}_i^s(\xi) + \hat{\mathbf{n}}^i(\xi)$ intersects with $\xi^r + k^r \mathbf{r}(\xi)$ at $\mathbf{q}_i^s(\xi)$ with $k^r \in \mathbb{R}$ (Fig. 22).

This allows to create a triangle spanned by the lines ξ , $\mathbf{p}_i^s(\xi)$ and $\mathbf{q}_i^s(\xi)$, colored in blue in Fig. 22. Using the associative law of the dot product, the geometry constraint of the blue triangle and (27), the maximum angle results in:

$$\langle \mathbf{n}^i, \mathbf{r} \rangle = \langle \hat{\mathbf{n}}^i, \mathbf{r} \rangle \geq \langle \xi - \mathbf{p}_i^s, \mathbf{r} \rangle \geq 0 \quad \forall w_i(\xi) > 0 \quad (47)$$

Hence the directional transformation of (11) results in $\|\kappa_i\| < \pi/2$, $\forall w_i(\xi) > 0$. Using additionally the *triangle equality* for vectors: $\|\kappa^1 + \kappa^2\| \leq \|\kappa^1\| + \|\kappa^2\|$ applied to all surface directions, it follows with (12) that:

$$\|\bar{\kappa}\| = \left\| \sum_{i=1}^{N^v} w^i \kappa^i \right\| \leq \sum_{i=1}^{N^v} w^i \|\kappa^i\| \leq \left(\sum_{i=1}^{N^v} w^i \right) \max_{i \text{ with } w^i > 0} \|\kappa^i\| \leq \frac{\pi}{2}$$

Since the basis vector of the directional mean is $\mathbf{r}(\xi)$, with (13) condition (46) holds true.

2) *Smooth Vector Field*: The continuous extension across the reference point is defined in Appendix B2 and applicable, too.

The reference direction $\mathbf{r}(\xi)$ and the distance function $\Gamma(\xi)$ does not have any other discontinuity.

The pseudo normal $\hat{\mathbf{n}}(\xi)$ is smoothly defined across space. Even the case when the edge point with the minimum is switching (25) no discontinuity occurs, since the angle will stay the same due to the flat surface.

3) *Applicability of General Proofs*: Since we have a smooth field of normal vectors $\mathbf{n}(\xi)$, we further need to define any smooth distance function which decreases its value with increasing distance. The two properties are sufficient to comply with the proof of Sec. B

D. Proof Theorem 4

To ensure impenetrability, the three cases described in (36) must be considered:

1) *Evaluation in Moving Frame*: $\dot{\xi} = \xi$

The simplest case comes with no stretching, but the evaluation in the local frame of the moving boundary of the obstacle. It follows that the Neuman-boundary condition for impenetrability holds (see also [32]).

2) *Contraction within Margin*: $\dot{\xi} = v_{max} \|\dot{\xi}\| \hat{\xi}$

This contraction is only performed, if it results in a normal velocity which is larger than the velocity of the obstacle $\dot{\xi}_o$, i.e. the evaluation in the moving frame results $\langle (\dot{\xi} - \dot{\xi}_o), \mathbf{n}(\xi) \rangle \geq 0$, hence ensuring impenetrability.

3) *Contraction in Tangent Direction*: $\dot{\xi} = v_{o,n} \mathbf{n}(\xi) +$

$$\sqrt{v_{max}^2 - \|\dot{\xi}_n\|^2} \mathbf{e}(\xi)$$

This limited contraction along the normal direction ensures that the velocity in normal direction remains equal to the obstacles' velocity. The evaluation of the Neuman boundary condition in the moving frame leads to:

$$\langle (v_{o,n} \mathbf{n}(\xi) + \sqrt{v_{max}^2 - \|\dot{\xi}_n\|^2} \mathbf{e}(\xi)) - \dot{\xi}_o, \mathbf{n}(\xi) \rangle = v_{o,n} - v_{o,n} = 0$$

using the definition of (35) and the fact that the normal $\mathbf{n}(\xi)$ and the tangent $\mathbf{e}(\xi)$ are orthogonal.

REFERENCES

- [1] H. J. S. Feder and J.-J. Slotine, "Real-time path planning using harmonic potentials in dynamic environments," in *Robotics and Automation, 1997. Proceedings., 1997 IEEE International Conference on*, IEEE, vol. 1, 1997, pp. 874–881.
- [2] S. M. Khansari-Zadeh and A. Billard, "Learning stable nonlinear dynamical systems with gaussian mixture models," *IEEE Transactions on Robotics*, vol. 27, no. 5, pp. 943–957, 2011.
- [3] L. E. Kavraki, P. Svestka, J.-C. Latombe, and M. H. Overmars, "Probabilistic roadmaps for path planning in high-dimensional configuration spaces," *IEEE transactions on Robotics and Automation*, vol. 12, no. 4, pp. 566–580, 1996.
- [4] S. M. LaValle and J. J. Kuffner Jr, "Rapidly-exploring random trees: Progress and prospects," 2000.
- [5] O. Brock and O. Khatib, "Elastic strips: A framework for motion generation in human environments," *The International Journal of Robotics Research*, vol. 21, no. 12, pp. 1031–1052, 2002.
- [6] D. Ferguson, N. Kalra, and A. Stentz, "Replanning with rrts," in *Robotics and Automation, 2006. ICRA 2006. Proceedings 2006 IEEE International Conference on*, IEEE, 2006, pp. 1243–1248.
- [7] J. Vannoy and J. Xiao, "Real-time adaptive motion planning (ramp) of mobile manipulators in dynamic environments with unforeseen changes," *IEEE Transactions on Robotics*, vol. 24, no. 5, pp. 1199–1212, 2008.

- [8] S. Murray, W. Floyd-Jones, Y. Qi, D. J. Sorin, and G. Konidaris, "Robot motion planning on a chip," in *Robotics: Science and Systems*, 2016.
- [9] J. Ji, A. Khajepour, W. W. Melek, and Y. Huang, "Path planning and tracking for vehicle collision avoidance based on model predictive control with multiconstraints," *IEEE Transactions on Vehicular Technology*, vol. 66, no. 2, pp. 952–964, 2017.
- [10] X. Zhang, A. Liniger, and F. Borrelli, "Optimization-based collision avoidance," *IEEE Transactions on Control Systems Technology*, 2020.
- [11] O. Arslan and D. E. Koditschek, "Exact robot navigation using power diagrams," in *Robotics and Automation (ICRA), 2016 IEEE International Conference on*, IEEE, 2016, pp. 1–8.
- [12] J. Michels, A. Saxena, and A. Y. Ng, "High speed obstacle avoidance using monocular vision and reinforcement learning," in *Proceedings of the 22nd international conference on Machine learning*, ACM, 2005, pp. 593–600.
- [13] P. Long, W. Liu, and J. Pan, "Deep-learned collision avoidance policy for distributed multiagent navigation," *IEEE Robotics and Automation Letters*, vol. 2, no. 2, pp. 656–663, 2017.
- [14] O. Khatib, "Real-time obstacle avoidance for manipulators and mobile robots," *The international journal of robotics research*, vol. 5, no. 1, pp. 90–98, 1986.
- [15] D. E. Koditschek and E. Rimon, "Robot navigation functions on manifolds with boundary," *Advances in applied mathematics*, vol. 11, no. 4, pp. 412–442, 1990.
- [16] E. Rimon and D. E. Koditschek, "The construction of analytic diffeomorphisms for exact robot navigation on star worlds," *Transactions of the American Mathematical Society*, vol. 327, no. 1, pp. 71–116, 1991.
- [17] H. Kumar, S. Paternain, and A. Ribeiro, "Navigation of a quadratic potential with ellipsoidal obstacles," in *2019 IEEE 58th Conference on Decision and Control (CDC)*, IEEE, 2019, pp. 4777–4784.
- [18] A. Duan, R. Camoriano, D. Ferigo, Y. Huang, D. Caltandriello, L. Rosasco, and D. Pucci, "Learning to avoid obstacles with minimal intervention control," *Frontiers in Robotics and AI*, vol. 7, 2020.
- [19] E. Rimon and D. E. Koditschek, "Exact robot navigation using artificial potential functions," *IEEE Transactions on robotics and automation*, vol. 8, no. 5, pp. 501–518, 1992.
- [20] S. Paternain, D. E. Koditschek, and A. Ribeiro, "Navigation functions for convex potentials in a space with convex obstacles," *IEEE Transactions on Automatic Control*, 2017.
- [21] S. G. Loizou, "The navigation transformation," *IEEE Transactions on Robotics*, vol. 33, no. 6, pp. 1516–1523, 2017.
- [22] —, "Closed form navigation functions based on harmonic potentials," in *Decision and Control and European Control Conference (CDC-ECC), 2011 50th IEEE Conference on*, IEEE, 2011, pp. 6361–6366.
- [23] C. I. Connolly, J. B. Burns, and R. Weiss, "Path planning using laplace's equation," in *Robotics and Automation, 1990. Proceedings., 1990 IEEE International Conference on*, IEEE, 1990, pp. 2102–2106.
- [24] J.-O. Kim and P. K. Khosla, "Real-time obstacle avoidance using harmonic potential functions," *IEEE Transactions on Robotics and Automation*, vol. 8, no. 3, pp. 338–349, 1992.
- [25] J. Guldner and V. I. Utkin, "Sliding mode control for an obstacle avoidance strategy based on a harmonic potential field," in *Decision and Control, 1993., Proceedings of the 32nd IEEE Conference on*, IEEE, 1993, pp. 424–429.
- [26] S. M. Khansari-Zadeh and A. Billard, "A dynamical system approach to realtime obstacle avoidance," *Autonomous Robots*, vol. 32, no. 4, pp. 433–454, 2012.
- [27] M. Saveriano and D. Lee, "Distance based dynamical system modulation for reactive avoidance of moving obstacles," in *Robotics and Automation (ICRA), 2014 IEEE International Conference on*, IEEE, 2014, pp. 5618–5623.
- [28] P. Fiorini and Z. Shiller, "Motion planning in dynamic environments using velocity obstacles," *The International Journal of Robotics Research*, vol. 17, no. 7, pp. 760–772, 1998.
- [29] J. Van den Berg, M. Lin, and D. Manocha, "Reciprocal velocity obstacles for real-time multi-agent navigation," in *2008 IEEE International Conference on Robotics and Automation*, IEEE, 2008, pp. 1928–1935.
- [30] D. Wilkie, J. Van Den Berg, and D. Manocha, "Generalized velocity obstacles," in *2009 IEEE/RSJ International Conference on Intelligent Robots and Systems*, IEEE, 2009, pp. 5573–5578.
- [31] L. Zhang, J. Wang, Z. Lin, L. Lin, Y. Chen, and B. He, "Distributed cooperative obstacle avoidance for mobile robots using independent virtual center points," *Journal of Intelligent & Robotic Systems*, pp. 1–15, 2019.
- [32] L. Huber, A. Billard, and J.-J. Slotine, "Avoidance of convex and concave obstacles with convergence ensured through contraction," *IEEE Robotics and Automation Letters*, vol. 4, no. 2, pp. 1462–1469, 2019.
- [33] S. Khansari-Zadeh, *A dynamical system-based approach to modeling stable robot control policies via imitation learning*, PhD Thesis, 2012.
- [34] M. Khoramshahi and A. Billard, "A dynamical system approach to task-adaptation in physical human-robot interaction," *Autonomous Robots*, pp. 1–20, 2018.
- [35] D. F. P. Granados, H. Kadone, and K. Suzuki, "Unpowered lower-body exoskeleton with torso lifting mechanism for supporting sit-to-stand transitions," in *2018 IEEE/RSJ International Conference on Intelligent Robots and Systems (IROS)*, IEEE, 2018, pp. 2755–2761.
- [36] F. Grzeskowiak, M. Babel, J. Bruneau, and J. Pettré, "Toward virtual reality-based evaluation of robot navigation among people," in *2020 IEEE Conference on Virtual Reality and 3D User Interfaces (VR)*, IEEE, 2020, pp. 766–774.
- [37] D. Jia, A. Hermans, and B. Leibe, "Dr-spaam: A spatial-attention and auto-regressive model for person detection in 2d range data," in *2020 IEEE/RSJ International*

- Conference on Intelligent Robots and Systems (IROS)*, 2020, pp. 10 270–10 277. DOI: 10.1109/IROS45743.2020.9341689.
- [38] N. Das and M. Yip, “Learning-based proxy collision detection for robot motion planning applications,” *IEEE Transactions on Robotics*, 2020.
- [39] A. D. Ames, S. Coogan, M. Egerstedt, G. Notomista, K. Sreenath, and P. Tabuada, “Control barrier functions: Theory and applications,” in *2019 18th European Control Conference (ECC)*, IEEE, 2019, pp. 3420–3431.
- [40] A. Taylor, A. Singletary, Y. Yue, and A. Ames, “Learning for safety-critical control with control barrier functions,” in *Learning for Dynamics and Control*, PMLR, 2020, pp. 708–717.
- [41] R. Cheng, G. Orosz, R. M. Murray, and J. W. Burdick, “End-to-end safe reinforcement learning through barrier functions for safety-critical continuous control tasks,” in *Proceedings of the AAAI Conference on Artificial Intelligence*, vol. 33, 2019, pp. 3387–3395.